Supplementary Information (SI) for Journal of Materials Chemistry A.

Supplementary Information for

Synergistic effect of morphology evolution with oxygen vacancies on layered cathode derived from polyoxovanadates for aqueous zinc-ion batteries

Yu-Ying Yang[a, 1], Si-Yu Chen[a, 1], Yong-Jia Ding[a], Yun-Xiang Zhou[a], Huan He[a], Qiaoji Zheng[a], Rui Zhang[b,*], Dunmin Lin[a], Yu Huo[a,c*]

[a] College of Chemistry and Materials Science, Sichuan Normal University, Chengdu 610066, P. R. China

[b] School of Chemical and Environmental Engineering, Shanghai Institute of Technology, Shanghai, 201418, PR China

[c] Key Laboratory of Advanced Energy Materials Chemistry (Ministry of Education), Nankai University, Tianjin 300071, China

[1] These authors contributed equally to this work.

Contents:

1. Experimental Section

1.1 Materials and methods

V_2O_5 (99%), $(N_2H_5)_2SO_4$ (99.5%), $FeSO_4\cdot 7H_2O$ (99%) and $Zn(CF_3SO_3)_2$ (98.0%) were purchased from Shanghai Macklin Biochemical Technology. $LiOH\cdot H_2O$ (99%), HCl (36%), N-methylpyrrolidone (NMP, 99.9%), ethanol, and polyvinylidene fluoride (PVDF) were all obtained from National Medicine Chemical Reagent Co, Ltd. Single-layer graphene oxide (flake diameter: 0.5-5 μm, thickness: 0.8-1.2 nm, Xianfeng Nanotechnology Co., Ltd, China).

X-ray diffraction powder pattern (XRD) was obtained on a Miliflex diffractometer with Cu-Kα radiation (λ= 1.54 Å) and recorded in the range of 5-60° with a scanning rate of 6° min^{-1}. The Raman scattering spectra were acquired on a Renishaw InVia system (532 nm Laser). The specific surface area and pore property of samples were obtained by the multipoint Brunauer- Emmett-Teller (BET, ASAP2020HD8 Surface Area and Porosity Analyzer) analysis based on the N_2 adsorption-desorption isotherms principle. X-ray photoelectron spectroscopy (XPS, ESCALAB Xi) was gained with an Al-Kα radiation source. The electron paramagnetic resonance (EPR) spectrum was obtained using Bruker EMXplus. The morphology and microstructure of the samples were analyzed by scanning electron microscopy (SEM, Zeiss/sigma 500) and transmission electron microscopy (TEM, JEOL JEM-2100 F).

1.2 Synthesis

1.2.1. Synthesis of $[Fe_3V_{18}O_{42}(H_2O)_{12}(VO_4)]\cdot 24H_2O$ (Fe_3V_{18})

Fe_3V_{18} was synthesized based on literature [1]. V_2O_5 (5.4564 g, 0.03 mol) was dissolved in distilled water (160 mL) and heated to 85 °C, and then the solution (36 mL) containing

$LiOH\cdot H_2O$ solution (2.5176 g, 0.06 mol) and $(N_2H_5)_2SO_4$ (3.9036 g, 0.03 mol) was added. Subsequently, the resulting solution was diluted to 300 mL and then the pH was adjusted to 4.6 with 2 M HCl. After that, $FeSO_4\cdot 7H_2O$ (4.1703 g, 0.015 mol) was added to the above solution and stirred for 5 h. The final crystalline product was obtained by slow evaporation at room temperature after 12 h.

1.2.2. Synthesis of $[Fe_5V_{15}O_{39}(OH)_9]\cdot 9H_2O$ (FeVO)

GO (0.02 g) was ultrasonically dispersed in distilled water, and the solution (60 mL) with Fe_3V_{18} precursor (0.252 g) was added dropwise. The resulting suspension was transferred to a 100 mL Teflon-lined autoclave and maintained at 180 °C for 24 h. After cooling to room temperature, the black FeVO-R was obtained.

As a comparison, FeVO-B was synthesized under the same conditions without adding GO.

1.3 Electrochemical tests

The cathode slurry was prepared by mixing the active materials, acetylene black, and PVDF binder in a moderate amount of NMP solvent at a mass ratio of 7:2:1, then the obtained slurry was coated on titanium foil (2 mm) with a mass loading of 1 mg cm^{-2} and dried in a vacuum oven at 60 °C for 12 h. The button cells (CR2032) were assembled in air using zinc foil as the anode, 2 M $Zn(CF_3SO_3)_2$ as electrolyte, and glass fiber as separator. Constant current charge-discharge tests were executed on a LAND CT2100A battery testing system in the voltage range of 0.2-1.6 V. The cyclic voltammetry curves (CV) and electrochemical impedance spectroscopy (EIS) were performed on the CHI 760E electrochemical workstation. The Galvanostatic intermittent titration technique (GITT) was performed at 0.1 A g^{-1} with a constant current charge of 5 min and the relaxation of 10 min, severally.

2. Supplementary Measurement

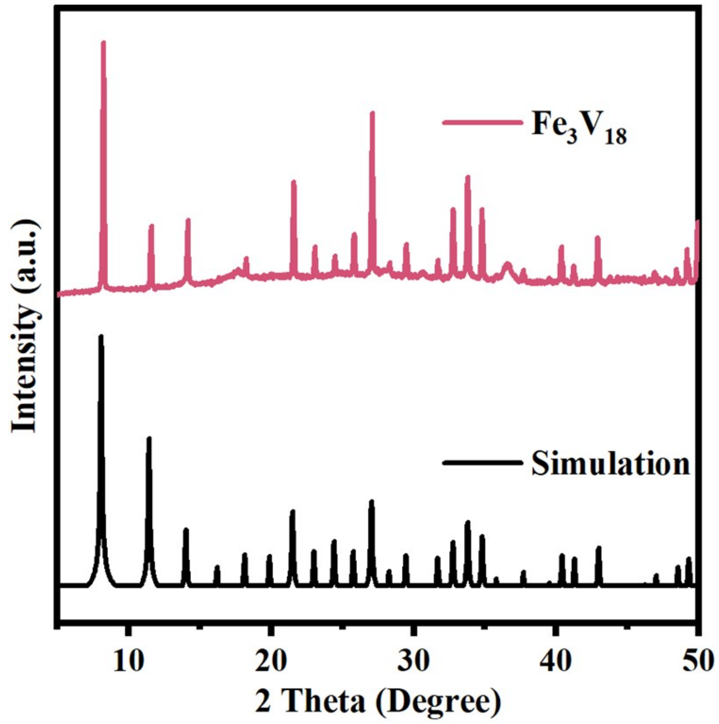

Figure S1. Experimental and simulated X-ray powder diffraction patterns for Fe_3V_{18}.

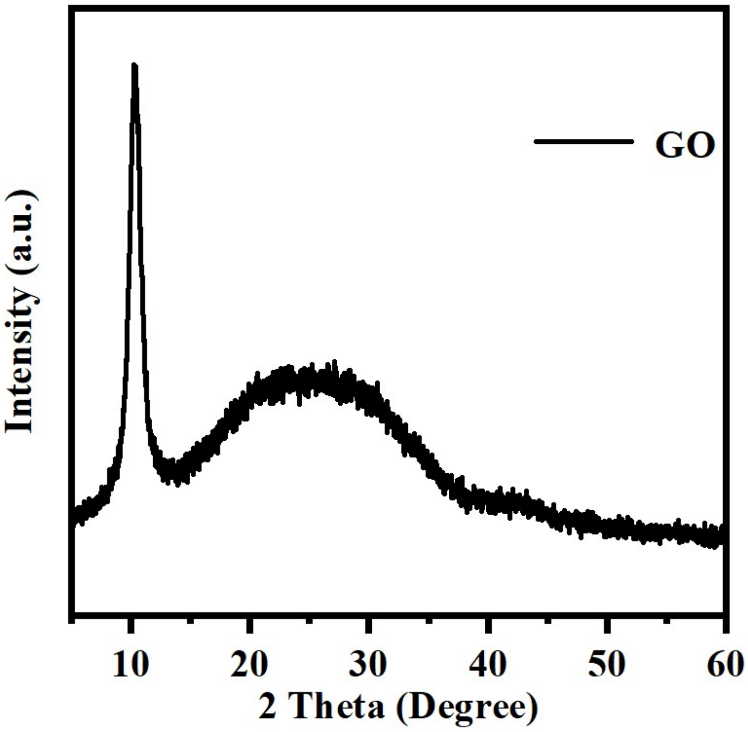

Figure S2. X-ray powder diffraction patterns for GO.

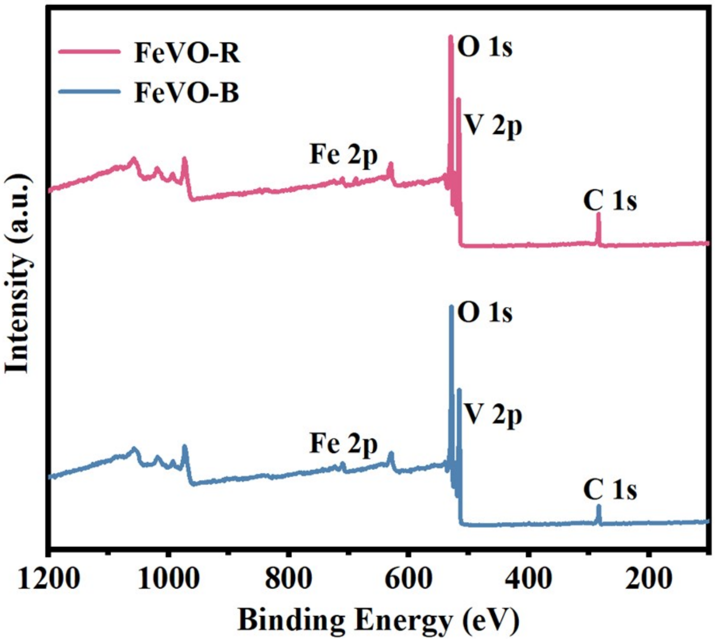

Figure S3. XPS survey spectra of FeVO-R and FeVO-B.

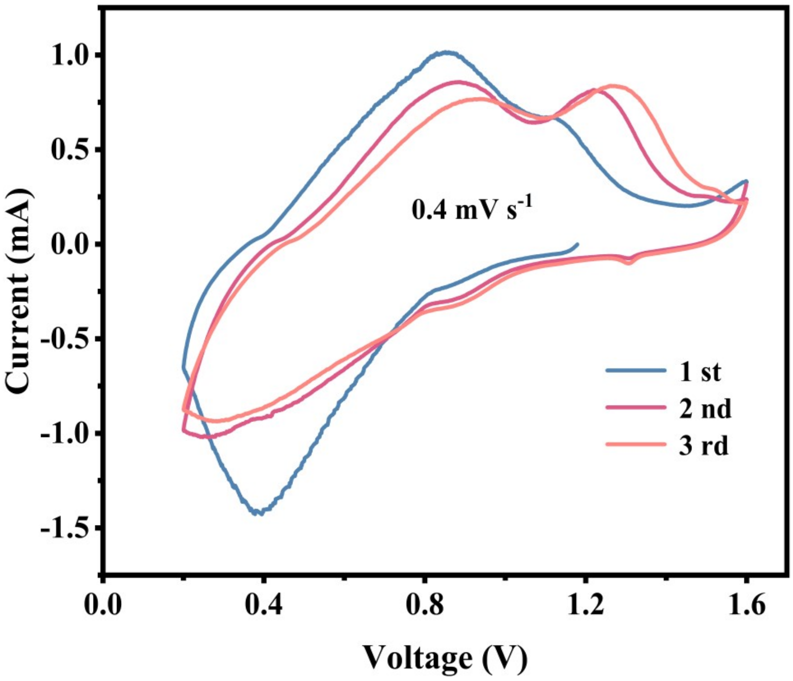

Figure S4. CV curves of FeVO-B at 0.4 mV s^{-1}.

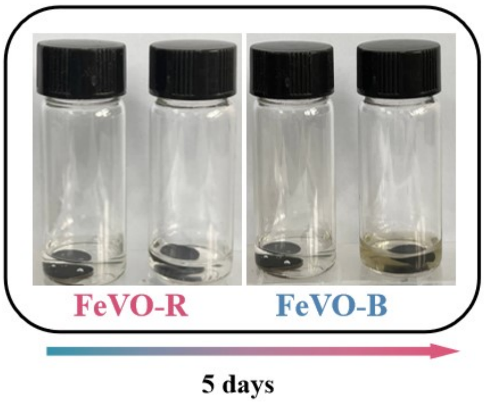

Figure S5. Optical images of pristine FeVO-R and FeVO-B electrodes immersed in 2 M $Zn(CF_3SO_3)_2$ electrolyte for 5d.

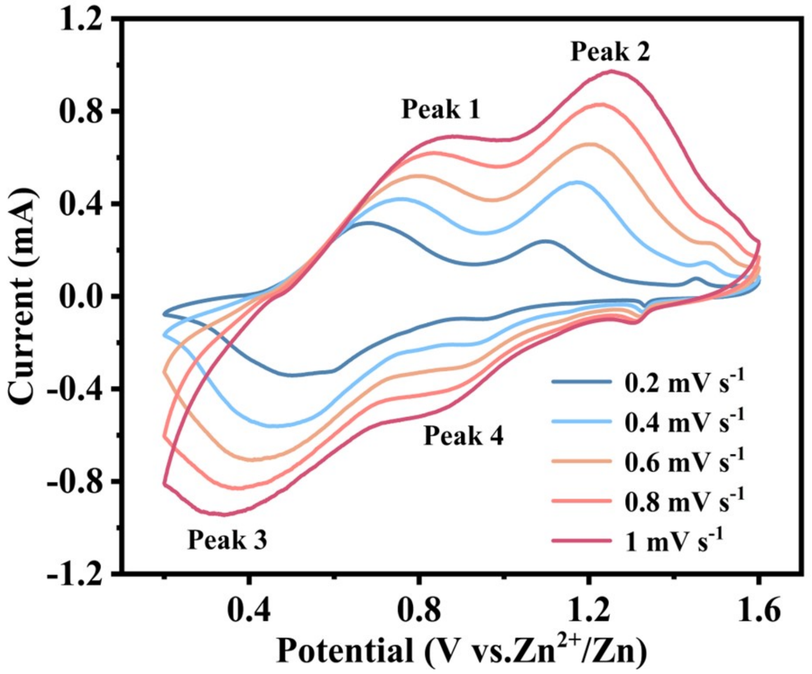

Figure S6. CV curves of the FeVO-B at different scan rates.

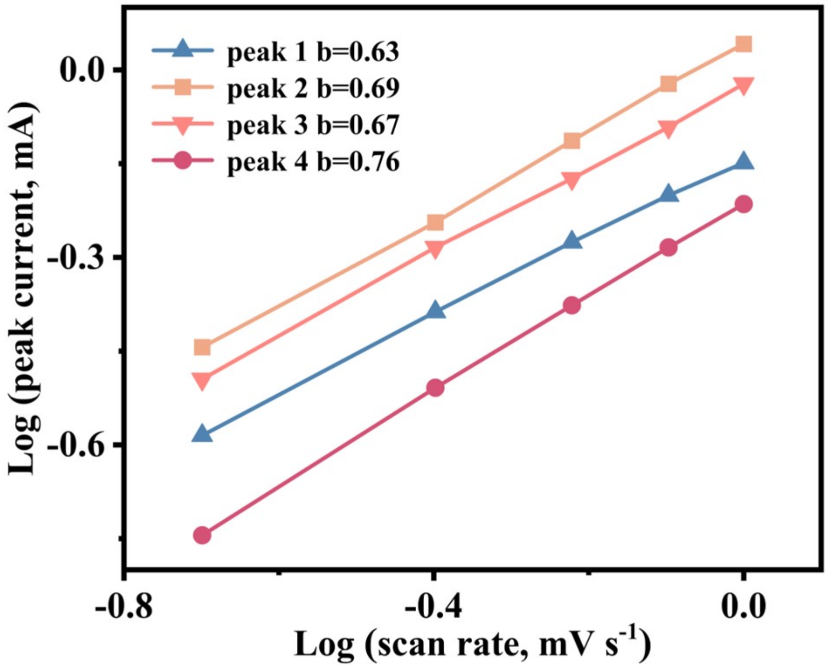

Figure S7. Relationship between log *i* and log *v* at specific peak currents for FeVO-B.

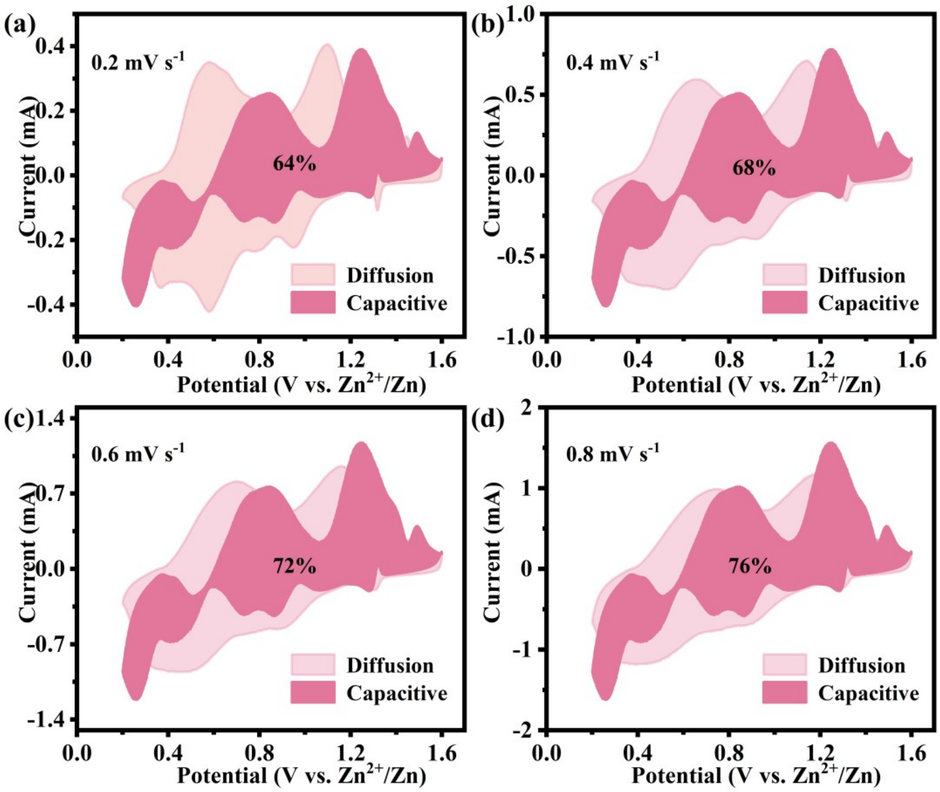

Figure S8. Capacitive contribution at (a) 0.2 mV s^{-1}, (b) 0.4 mV s^{-1}, (c) 0.6 mV s^{-1} and (d) 0.8 mV s^{-1} for FeVO-R.

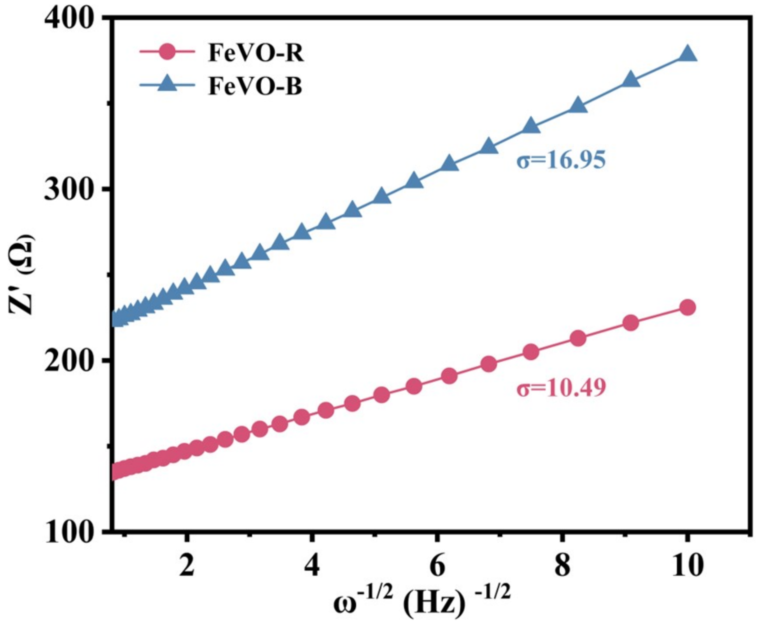

Figure S9. Linear relationship between Z′ and $\omega^{-1/2}$ of FeVO-R and FeVO-B.

3. Theoretical calculations

All of the calculations are performed in the framework of the spin-polarized density functional theory with the projector augmented plane-wave method, as implemented in the Vienna ab initio simulation package (VASP) [2,3]. The generalized gradient approximation (GGA) proposed by Perdew, Burke, and Ernzerhof (PBE) is selected for the exchange-correlation potential [4,5]. The long-range van der Waals interaction is described by the DFT-D3 approach [6]. The cut-off energy for plane wave is set to 480 eV. The energy criterion is set to 10^{-4} eV in iterative solution of the Kohn-Sham equation. All the structures are relaxed until the residual forces on the atoms have declined to less than 0.05 eV/Å. Data analysis and visualization are carried out with the help of VASPKIT [7] code and VESTA [8]. The diffusion barrier of adsorbed hydrogen at different adsorption sites were explored by using the Nudge Elastic Band (CI-NEB) method [9].

The adsorption energy Eads is expressed as:

$$\Delta E_{\text{ads}}=E_{\text{A+B}}-E_{\text{A}}-E_{\text{B}}$$

where E_{A+B} is the total energy of slab A model with B adsorption, E_A is the energy of a A slab, and E_B is that for a B molecule.

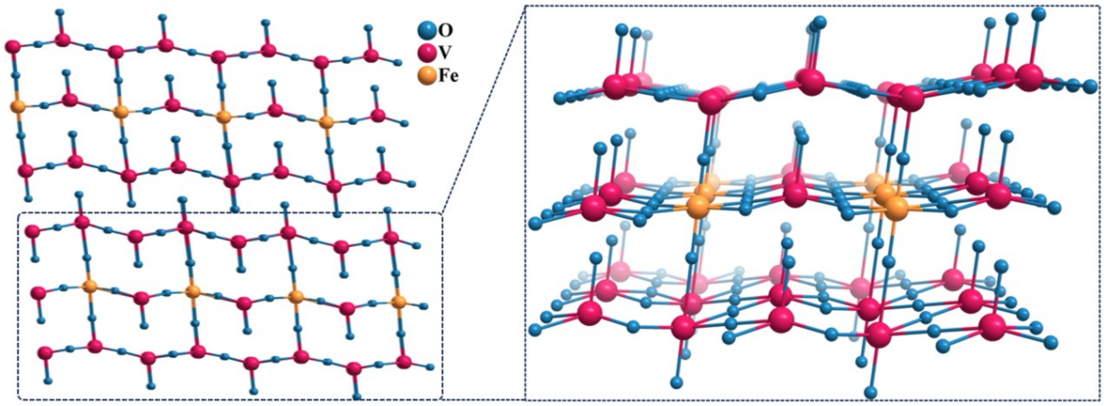

Figure S10. Theoretical models of FeVO.

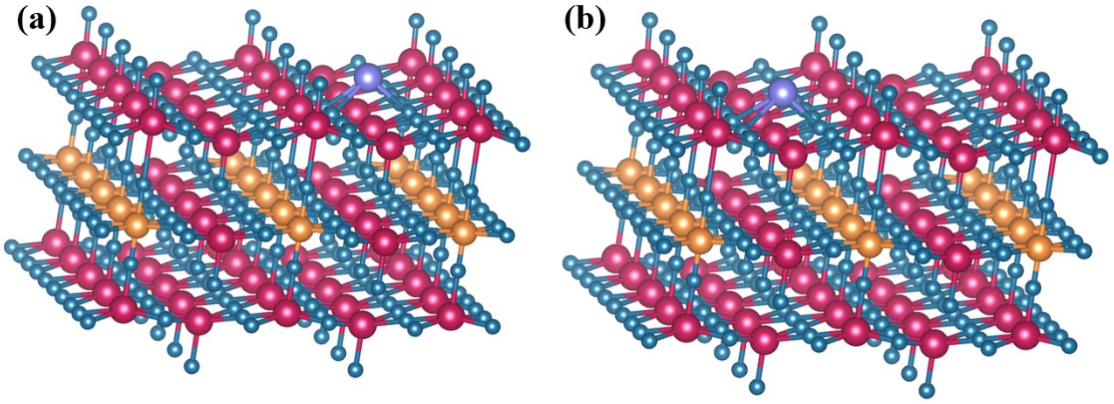

Figure S11. Structural diagrams of Zn^{2+} adsorbed on FeVO-B (a) and FeVO-R (b) cathodes.

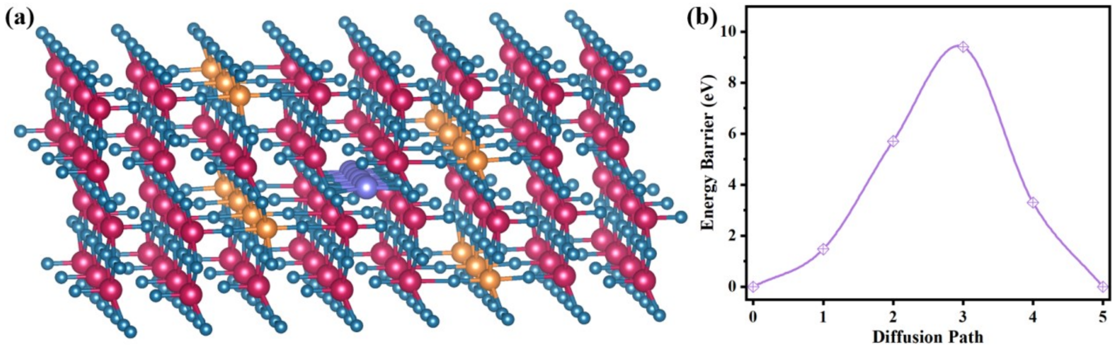

Figure S12. The migration pathways for Zn^{2+} between layers in FeVO (a) and the corresponding Zn^{2+} diffusion barriers (b).

4. Zinc ion storage mechanism

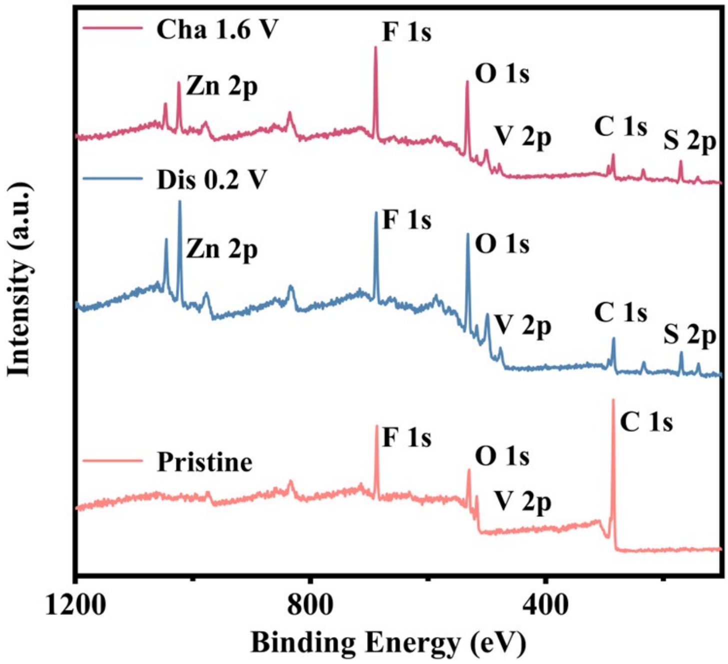

Figure S13. All-elements XPS spectra of FeVO-R at different charging and discharging states.

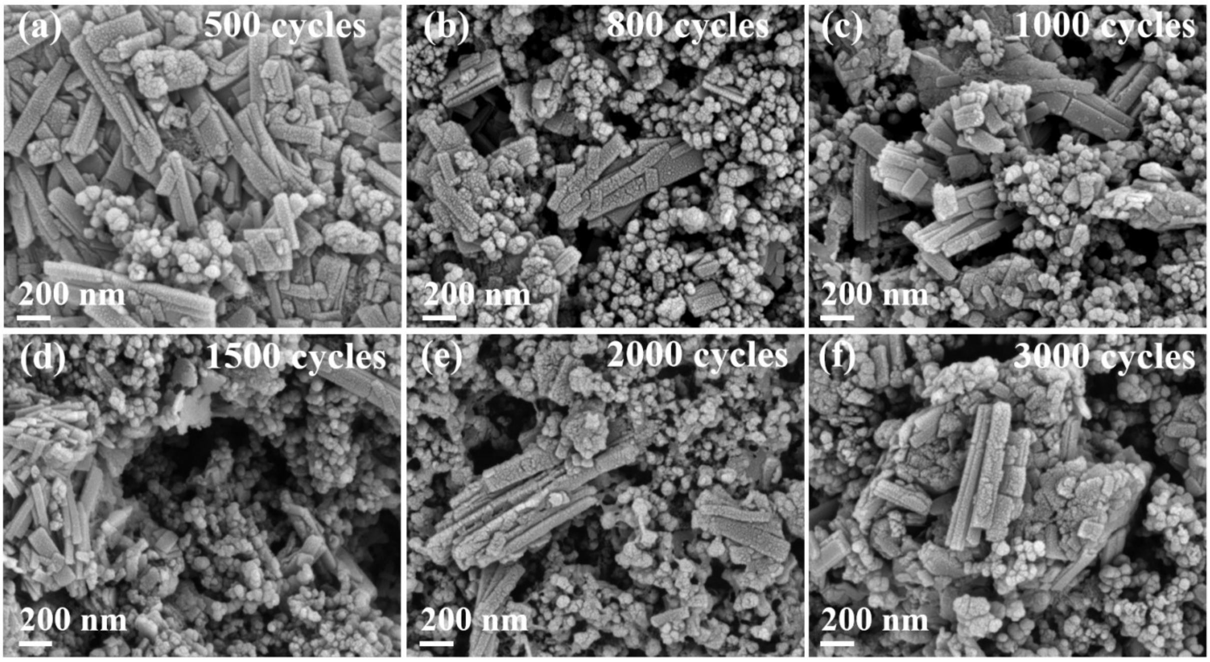

Figure S14. SEM images of FeVO-R electrode charged to 1.6 V at 500th (a), 800th (b), 1000th (c), 1500th (d), 2000th (e), 3000th (f) cycles.

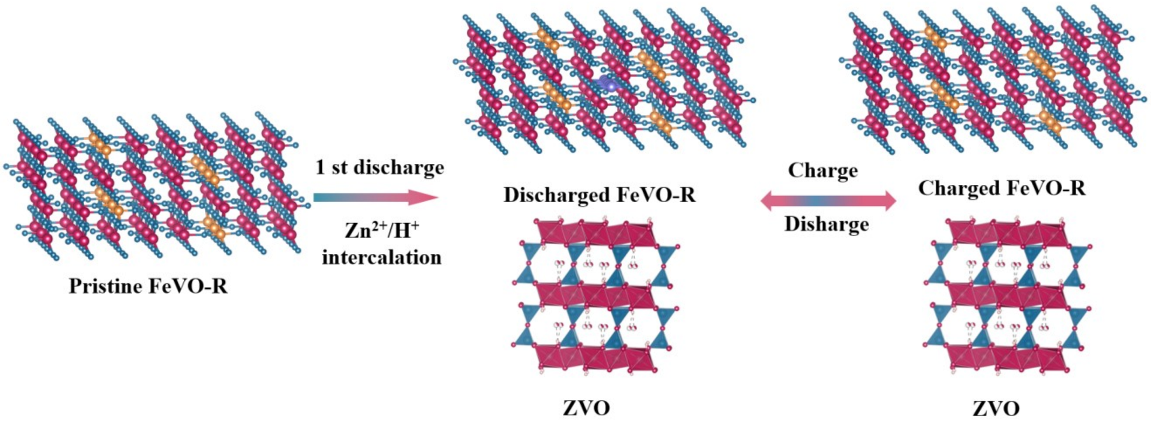

Figure S15. Diagram of Zn^{2+} ion storage mechanism in FeVO-R.

Table S1. Vanadium-based materials used as electrode materials for zinc-ion batteries.

Electrode materials	Capacity				Ref
	0.1 A g^{-1}	0.2 A g^{-1}	0.5 A g^{-1}	5 A g^{-1}	
This work	**409 mAh g^{-1}**	**374 mAh g^{-1}**	**356 mAh g^{-1}**	**208 mAh g^{-1}**	
CS@ZVO	323 mAh g^{-1}	278 mAh g^{-1}	242 mAh g^{-1}	97 mAh g^{-1}	**S10**
$Ag_2V_4O_{11}$	/	210 mAh g^{-1}	182 mAh g^{-1}	111 mAh g^{-1}	**S11**
VN_xO_y	310 mAh g^{-1}	291 mAh g^{-1}	276 mAh g^{-1}	204 mAh g^{-1}	**S12**
O_v-ZVO	402 mAh g^{-1}	365 mAh g^{-1}	345 mAh g^{-1}	/	**S13**
$K_{0.5}VOPO_4·1.5H_2O$	181 mAh g^{-1}	166 mAh g^{-1}	151 mAh g^{-1}	107 mAh g^{-1}	**S14**
V_2O_5@PEDOT	293 mAh g^{-1}	/	224 mAh g^{-1}	110 mAh g^{-1}	**S15**
VO@pAP	383 mAh g^{-1}	331 mAh g^{-1}	276 mAh g^{-1}	139 mAh g^{-1}	**S16**

References

[1] F.-C. Shen, C. Guo, S.-N. Sun, Z. Lei, Y.-Q. Lan, Self-Sacrificing Template of the POMs-Based Composite for the High-Performance Organic–Inorganic Hybrid Cathode of Lithium-Ion Batteries, *Inorg. Chem*, 61 (2022) 11182-11188.

[2] Kresse, G. & Hafner, J. Ab initio molecular dynamics for open-shell transition metals. *Phys. Rev. B*, 48 (1993) 13115-13118.

[3] Kresse, G. F. l., J. Efficient iterative schemes for ab initio total-energy calculations using a plane-wave basis set. *Phys. Rev. B*, 54 (1996) 169-185.

[4] John P. Perdew, K. B., and Matthias Ernzerhof. Generalized gradient approximation made simple. *Phys. Rev. Lett*, 77 (1996) 3865.

[5] Kohn, W. & Sham, L. J. Self-Consistent Equations Including Exchange and Correlation Effects. *Phys. Rev*, 140 (1965) A1133-A1138.

[6] Grimme, S., Antony, J., Ehrlich, S. & Krieg, H. A consistent and accurate ab initio parametrization of density functional dispersion correction (DFT-D) for the 94 elements H-Pu. *J. Chem. Phys*, 132 (2010) 154104.

[7] Wang, V., Xu, N., Liu, J.-C., Tang, G. & Geng, W.-T. VASPKIT: A user-friendly interface facilitating high-throughput computing and analysis using VASP code. *Comput. Phys. Commun*, 267 (2021) 108033.

[8] Momma, K. & Izumi, F. VESTA: a three-dimensional visualization system for electronic and structural analysis. *J. Appl. Crystallogr*, 41 (2008) 653-658.

[9] Henkelman G, Uberuaga B P, Jónsson H. A climbing image nudged elastic band method for finding saddle points and minimum energy paths. *J. Chem. phys*, 113 (2000) 9901-9904.

[10] J. Yang, J. Li, Y. Li, Z. Wang, L. Ma, W. Mai, M. Xu, L. Pan, Defect regulation in bimetallic oxide cathodes for significantly improving the performance of flexible aqueous Zn-ion batteries, *Chem. Eng. J*, 468 (2023) 143600.

[11] Q. Li, Y. Liu, K. Ma, G. Yang, C. Wang, In Situ Ag Nanoparticles Reinforced Pseudo-Zn-Air Reaction Boosting $Ag_2V_4O_{11}$ as High-Performance Cathode Material for Aqueous Zinc-Ion Batteries, *Small Methods* 3 (2019) 1900637.

[12] X. Xie, G. Fang, W. Xu, J. Li, M. Long, S. Liang, G. Cao, A. Pan, In Situ Defect Induction in Close-Packed Lattice Plane for the Efficient Zinc Ion Storage, *Small* 17 (2021) 2101944.

[13] J.J. Ye, P.H. Li, H.R. Zhang, Z.Y. Song, T. Fan, W. Zhang, J. Tian, T. Huang, Y. Qian, Z. Hou, N. Shpigel, L.F. Chen, S.X. Dou, Manipulating Oxygen Vacancies to Spur Ion Kinetics in V_2O_5 Structures for Superior Aqueous Zinc-Ion Batteries, *Adv. Funct. Mater*, 33 (2023) 2305659.

[14] L. Wang, M. Zhao, X. Zhang, M. Wu, Y. Zong, Y. Chen, X. Huang, M. Xing, X. Ning, W. Wen, D. Zhu, X. Ren, Novel high-voltage cathode for aqueous zinc ion batteries: Porous $K_{0.5}VOPO_4 \cdot 1.5H_2O$ with reversible solid-solution intercalation and conversion storage mechanism, *J. Energy Chem*, 93 (2024) 71-78.

[15] T. Yang, D. Xin, N. Zhang, J. Li, X. Zhang, L. Dang, Q. Li, J. Sun, X. He, R. Jiang, Z. Liu, Z. Lei, Interfacial polymerization of PEDOT sheath on V_2O_5 nanowires for stable aqueous zinc ion storage, *J. Mater. Chem. A*, 12 (2024) 10137-10147.

[16] Z. Song, Y. Zhao, A. Zhou, H. Wang, X. Jin, Y. Huang, L. Li, F. Wu, R. Chen, Organic Intercalation Induced Kinetic Enhancement of Vanadium Oxide Cathodes for Ultrahigh-Loading Aqueous Zinc-Ion Batteries, *Small* 20 (2023) 2305030.